Elliptic flow of charged pions, protons and strange particles emitted in Pb+Au collisions at top SPS energy[☆]

D. Adamová[a], G. Agakichiev[b,k], A. Andronic[c,l], D. Antończyk[d], H. Appelshäuser[d], V. Belaga[b],
J. Bielčíková[e,f,m], P. Braun-Munzinger[c,l], O. Busch[f], A. Cherlin[g], S. Damjanović[f], T. Dietel[h],
L. Dietrich[f], A. Drees[i], W. Dubitzky[f], S. I. Esumi[f,n], K. Filimonov[f,o], K. Fomenko[b],
Z. Fraenkel[g,*], C. Garabatos[c], P. Glässel[f], G. Hering[c], J. Holeczek[c], M. Kalisky[c], G. Krobath[f],
V. Kushpil[a], A. Maas[c], A. Marín[c,l], J. Milošević[f,p], D. Miśkowiec[c,l], Y. Panebrattsev[b],
O. Petchenova[b], V. Petráček[f,q], S. Radomski[c], J. Rak[c,r], I. Ravinovich[g], P. Rehak[j,*], H. Sako[c],
W. Schmitz[f], S. Schuchmann[d], S. Sedykh[c], S. Shimansky[b], J. Stachel[f], M. Šumbera[a],
H. Tilsner[f], I. Tserruya[g], G. Tsiledakis[c], J. P. Wessels[h], T. Wienold[f], J. P. Wurm[e], S. Yurevich[f,s],
V. Yurevich[b]

[a]*Nuclear Physics Institute, Academy of Sciences of the Chech Republic, 25068 Řež, Czech Republic*
[b]*Joint Institute of Nuclear Research, Dubna, 141980 Moscow Region, Russia*
[c]*Institut für Kernphysik, GSI, 64291 Darmstadt, Germany*
[d]*Institut für Kernphysik, Johann Wolfgang Goethe-Universität Frankfurt, 60438 Frankfurt, Germany*
[e]*Max-Planck-Institut für Kernphysik, 69117 Heidelberg, Germany*
[f]*Physikalisches Institut, Universität Heidelberg, 69120 Heidelberg, Germany*
[g]*Department of Particle Physics, Weizmann Institute, Rehovot, 76100 Israel*
[h]*Institut für Kernphysik, Universität Münster, 48149 Münster, Germany*
[i]*Department for Physics and Astronomy, SUNY Stony Brook, NY 11974, USA*
[j]*Instrumentation Division, Brookhaven National Laboratory, Upton, NY 11973-5000, USA*
[k]*Present affiliation: II. Physikalisches Institut der Justus Liebig Universität, Giessen, Germany*
[l]*Present affiliation: Research Division and Extreme Matter Institute (EMMI), GSI Helmholtzzentrum für Schwerionenforschung, 64291 Darmstadt, Germany*
[m]*Present affiliation: Nuclear Physics Institute, Academy of Sciences of the Czech Republic, 25068 Řež, Czech Republic*
[n]*Present affiliation: Institute of Physics, University of Tsukuba, Tsukuba, Japan*
[o]*Present affiliation: Physics Department, University of California, Berkeley, CA 94720-7300, USA*
[p]*Present affiliation: Faculty of Physics and Vinča Institute of Nuclear Sciences, University of Belgrade, 11001 Belgrade, Serbia*
[q]*Present affiliation: Faculty of Nuclear Science and Engineering, Czech Technical University, Prague, Czech Republic*
[r]*Present affiliation: Department of Physics, University of Jyväskylä, Jyväskylä, Finland*
[s]*Present affiliation: Institut für Kernphysik, GSI, 64291 Darmstadt, Germany*

Abstract

Differential elliptic flow spectra $v_2(p_T)$ of π^-, K_S^0, p, Λ have been measured at $\sqrt{s_{NN}}=$ 17.3 GeV around midrapidity by the CERN-CERES/NA45 experiment in mid-central Pb+Au collisions (10% of σ_{geo}). The p_T range extends from about 0.1 GeV/c (0.55 GeV/c for Λ) to more than 2 GeV/c. Protons below 0.4 GeV/c are directly identified by dE/dx. At higher p_T, proton elliptic flow is derived as a constituent, besides π^+ and K^+, of the elliptic flow of positive pion candidates. This retrieval requires additional inputs: (i) of the particle composition, and (ii) of $v_2(p_T)$ of *positive* pions. For (i), particle ratios obtained by NA49 are adapted to CERES conditions; for (ii), the measured $v_2(p_T)$ of *negative* pions is substituted, assuming π^+ and π^- elliptic flow magnitudes to be sufficiently close. The $v_2(p_T)$ spectra are compared to ideal-hydrodynamics calculations. In synopsis of the series π^- - K_S^0 - p - Λ, flow magnitudes are seen to fall with decreasing p_T progressively even below hydro calculations with early kinetic freeze-out ($T_f=$ 160 MeV) leaving

1

not much time for hadronic evolution. The proton $v_2(p_T)$ data show a downward swing towards low p_T with excursions into negative v_2 values. The pion-flow isospin asymmetry observed recently by STAR at RHIC, invalidating in principle our working assumption, is found in its impact on proton flow bracketed from above by the direct proton flow data, and not to alter any of our conclusions. Results are discussed in perspective of recent viscous hydrodynamics studies which focus on late hadronic stages.

☆CERES Collaboration

∗*deceased*

Email addresses: `Jovan.Milosevic@cern.ch` (J. Milošević), `J.P.Wurm@mpi-hd.mpg.de` (J. P. Wurm)

1. Introduction

Among the prominent results from the Relativistic Heavy Ion Collider (RHIC) are observations of strong elliptic flow (1, 2, 3, 4) in non-central collisions characterised by azimuthally anisotropic particle yields in the plane transverse to the beam direction (5, 6, 7, 8). Elliptic flow is quantified by v_2, the second harmonic coefficient of the azimuthal particle distribution with respect to the reaction plane. The observations directly assert the importance of strong interactions among constituents of the expanding, hot and dense medium by which the geometrical anisotropy of the almond shaped overlap zone evolves into the momentum space anisotropy that is measured. This evolution is described by relativistic hydrodynamics (9). More specifically, the large v_2 values agreed surprisingly well with predictions of hydrodynamics without dissipation. This was interpreted as the early-time response of a locally equilibrated system of a very peculiar kind, the strongly interacting Quark Gluon Plasma (QGP), behaving as a nearly perfect liquid with a very small ratio η/s of shear viscosity to entropy density (10, 11).

From $\sqrt{s_{NN}}$ = 200 GeV at RHIC to $\sqrt{s_{NN}}$ = 2.76 TeV a bold step upward in nucleon-nucleon centre-of-mass energy was recently taken with the operation of the Large Hadron Collider (LHC). First measurements of elliptic flow in Pb+Pb collisions report $v_2(p_T)$ for charged hadrons of similar magnitude and shape than at comparable centralities at RHIC (12, 13, 14). The average v_2 is $\approx 20\%$ larger at the LHC but this increase is mainly due to the harder p_T spectrum at LHC energies. This is in agreement with hydrodynamic predictions extrapolated from RHIC data without change in the (very low) viscosity to entropy density (15, 16), as well as a hybrid calculation treating the QGP by ideal hydrodynamics and the late stages by a hadronic cascade model (17).

At the Super Proton Synchrotron (SPS) energy, $\sqrt{s_{NN}}$ = 17.3 GeV, elliptic flow magnitudes v_2 are about 30% lower than at RHIC. The differential flow data $v_2(p_T)$ at SPS (18, 19, 20), though strikingly similar in shape to the RHIC and LHC data, stay well below calculations of ideal hydrodynamics (21). It should be noted that even at the highest RHIC energy some significant deviations remain (22).

The failure of hydrodynamics at low energy, large impact parameters or large forward rapidities has been ascribed to insufficient number densities at very early collision stages that hamper thermalization (23). Strong dissipative effects are bound to set in after chemical freeze-out with growing mean free paths during the late hadronic expansion (10, 11, 24, 25).

We present differential elliptic flow data $v_2(p_T)$ of of strange particles Λ and K_S^0 for mid-central 158 AGeV Pb+Au collisions collected by the CERES/NA45 experiment at the SPS (26); of negative pions complementing earlier, more peripheral data (19, 27); and of protons directly measured at low p_T by dE/dx identification and retrieved at higher p_T from the measured elliptic flow data of positive pion candidates containing besides pions and protons also kaons. The latter task assumes charge-independent pion flow, at least to an accuracy allowing to substitute the *negative*-pion $v_2(p_T)$ measured for the *positive*-pion $v_2(p_T)$ required. The particle composition also needed for the retrieval is fixed by particle ratios from the NA49 Collaboration that are adapted to CERES conditions.

Elliptic flow data of identified particles as presented here are sparse at the SPS, especially for massive particles, and reaching down to low p_T. We foresee these data to contribute valuable information on late stages of collective expansion which has been characterized by rescattering in the 'hadronic corona' (28) as an interplay between strong radial flow, elliptic flow, and thermal motion set by the freeze-out temperature (21). The proton flow data may turn out worth our effort as a probe specifically sensitive to hadronic viscosity (29).

The assumed pion-flow isospin symmetry has recently been found invalidated by results of the

2

'beam energy scan' of the STAR Collaboration (30), in minimum-bias collisions at low $\sqrt{s_{NN}}$ and low p_T. The yet unknown centrality dependence of the effect will be discussed in view of diverse physics scenarios. As a worst case remedy, our *directly* measured proton-flow data provide an upper limit for the uncertainty in proton v_2 inflicted by the pion-flow asymmetry.

2. Experiment

The 158 AGeV Pb+Au data were collected with the upgraded CERES/NA45 spectrometer during the heavy-ion run in 2000 at the CERN SPS. The CERES spectrometer is axially symmetric around the beam direction and covers full azimuth at polar angles $7.7° ≤ \vartheta ≤ 14.7°$, corresponding to a pseudorapidity range $2.05 < \eta < 2.70$ close to midrapidity ($y_{mid} = 2.91$); it is thus very well suited for elliptic flow studies. A cross-section view of the spectrometer is shown in Fig. 1. A detailed description of the CERES experiment is given in (31).
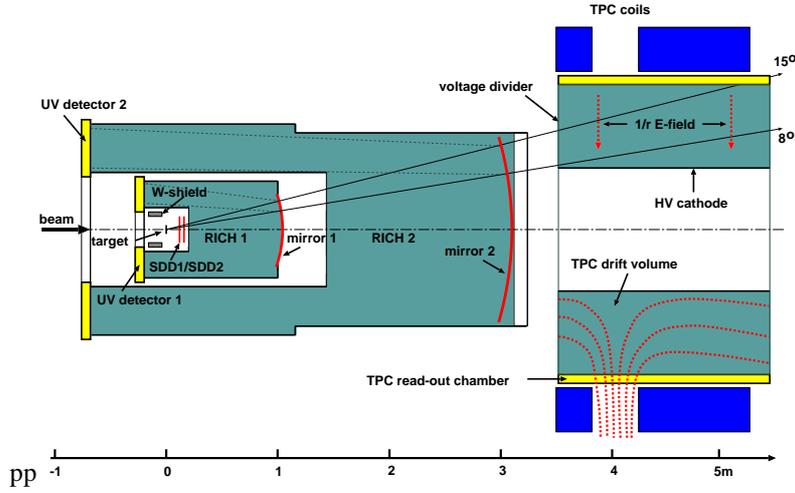

Figure 1: The CERES/NA45 spectrometer during final data taking in 2000.

The radial-drift Time Projection Chamber (TPC) (32) is operated inside a magnetic field with maximum radial component of 0.5 T, providing a precise determination of the momentum. Particle identification is achieved by the differential energy loss dE/dx along the tracks in the TPC. A doublet of radial Silicon Drift Detectors (SDD) (33), located at 10 and 13 cm downstream of a segmented Au target, is used for vertex reconstruction and tracking outside the field region. Charged particles emitted from the target are reconstructed by matching track segments in the SDD and in the TPC using a momentum-dependent matching window. The two Ring Imaging Cherenkov Counters (RICH1, RICH2) for electron identification were used in a previous CERES flow study of identified charged pions (19), but not in the measurement reported on here.

2.1. Momentum Resolution

The momentum is measured by determining the deflection of the tracks within the TPC. The momentum resolution is therefore depending on the spatial track resolution, but is degraded by multiple scattering in the detector material.

The results of an extensive Monte-Carlo study of the detector response were shown (34) to be well approximated by the simple expression

$$\Delta p/p = \sqrt{(2.0\%)^2 + (1.0\% \cdot p[\text{GeV/c}])^2}. \tag{1}$$

2.2. Trigger Samples

A sample of $30 \cdot 10^6$ events of 158 AGeV Pb+Au collisions was collected by a mixed-trigger selection with average centrality $\sigma/\sigma_{geo} = 5.5\%$; this choice was made to enhance e^+e^- production, CERES' main objective. The track-multiplicity distribution for 'all triggers', shown in Fig. 2 by squares, has an average track number $<N_{track}>_{|all} = 157.9$. It strongly deviates at low multiplicities from the minimum-bias distribution labeled (a) in Fig. 2: for the same average multiplicity, the minimum-bias distribution would have to be cut at $N_{track} = 129.1$ or at the top 11.4% of σ_{geo}.

The limited statistics of our strange-particle spectra allowed for only two centrality classes. The 'top-central' part matches the minimum-bias distribution almost to its cut off at $N_{track} = 159$ and comprises with $<N_{track}>_{|top} = 176.9$ the top central 2.4% of σ_{geo}. The remainder are 'mid-central' triggers, $<N_{track}>_{|mid} = 136.2$; these were used almost exclusively to collect the elliptic flow data. A precise definition of these triggers can only be provided by the distribution itself, together with the minimum-bias curve. For comparison to other experiments, we quote the slice cut from the minimum-bias distribution that has identical average multiplicity: it extends from 5.3% to 14.5% of σ_{geo} with a weighted average $\langle \sigma/\sigma_{geo} \rangle = 9.8\%$.

2.3. Pion and Proton Identification

Tracks in the TPC were reconstructed in the pseudorapidity range $2.05 \leq \eta \leq 2.70$. They had to pass quality cuts that required

- transverse momentum p_T above 50 MeV/c;

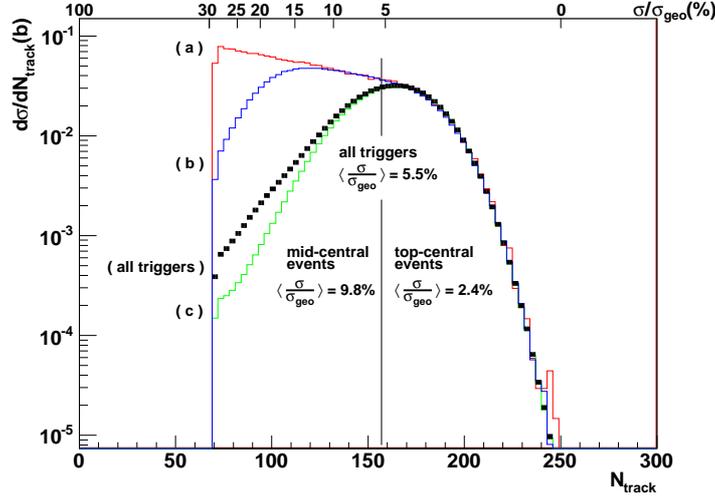- a minimum of 8 to 12 hits per track, depending on polar angle ϑ;

Figure 2: TPC track density for various trigger selections, (a) minimum-bias, (b) peripheral, (c) central. The combination of all triggers ('all triggers'), dominated by (c), has a weighted mean $\langle \sigma/\sigma_{geo} \rangle$ of 5.5 %. It is split into 'mid-central' triggers (left, $N_{track} < 159$) of 9.8 % by which most of the flow data were collected; and 'top-central' triggers (right, $N_{track} \geq 159$) of 2.4 %, respectively. The horizontal scale $\langle \sigma/\sigma_{geo} \rangle$ on top applies to (a) only. See text.
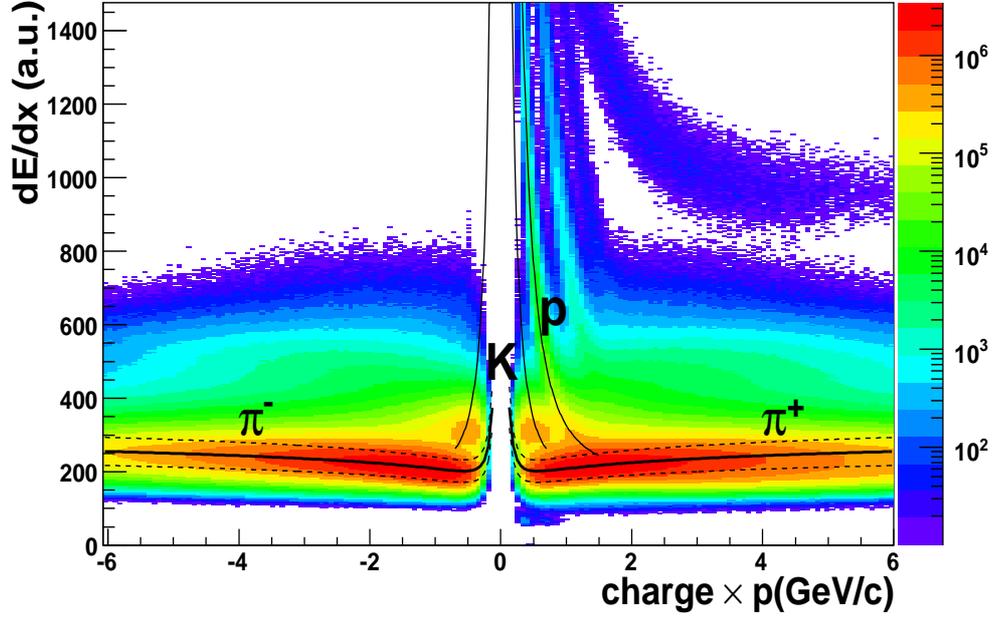
5

Figure 3: Contour plots of the specific energy loss of charged particles *vs* momentum times charge sign. Full lines show Bethe-Bloch energy loss for π, K, p, dashed lines the $\pm 1.5\sigma$ cut selecting pions. Relative dE/dx resolution, depending on number of hits per track, is typically 10%.

- TPC and SDD tracks of charged pions and primary protons to match within a $\pm 3\sigma$ p_T-dependent window.

Pion candidates are identified by their specific-energy loss sampled along the tracks in the TPC. On average, there are more than 10 hits per track.

In the two-dimensional scatter plot of Fig. 3, the measured specific energy loss dE/dx is shown as function of particle momentum p for both negative and positive charges. Shown are the cuts of Eq. 2 selecting pion candidates in a $\pm 1.5\sigma$, i.e. $\pm 15\%$, window (dashed lines) around the nominal energy loss for charged pions according to the Bethe-Bloch (BB) formula (full lines). The dE/dx cut is defined as

$$0.85 \frac{\mathrm{d}E}{\mathrm{d}x}(p, \pi^{\pm})\,|_{\mathrm{BB}} \leq \frac{\mathrm{d}E}{\mathrm{d}x}(p)\,|_{\mathrm{measured}} \leq 1.15 \frac{\mathrm{d}E}{\mathrm{d}x}(p, \pi^{\pm})\,|_{\mathrm{BB}} . \qquad (2)$$

Also shown are the Bethe-Bloch lines for kaons and protons, and it is obvious that over extended ranges in momentum pions will be mixed with kaons and protons, in case of positive charge. Antiprotons are only about 6% of protons at mid-rapidity. At very low momenta protons are well identified by dE/dx as can be observed from Fig. 4.

2.4. Reconstruction of Λ and K_S^0

The Λ particles are reconstructed via the decay channel $\Lambda \rightarrow p + \pi^-$ with branching ratio $BR = 63.9\%$ and mean decay length $c\tau = 7.89$ cm (35). Particle identification is performed
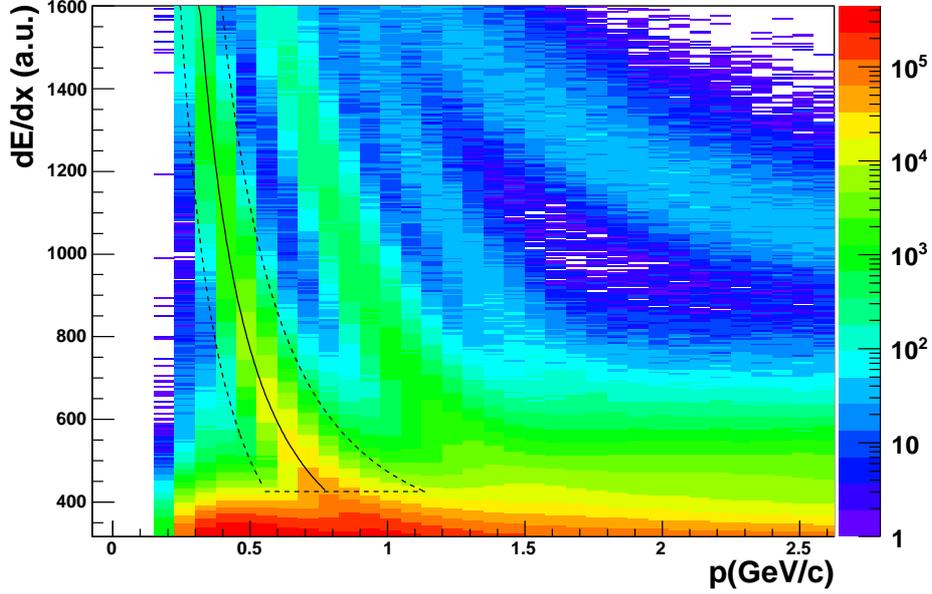
Figure 4: The low momentum part of Fig. 3 for positive charges with lines indicating the cut to select protons.

using the dE/dx samples from the TPC by applying a $\pm1.5\sigma$ and $\pm1.0\sigma$ window around the momentum dependent Bethe-Bloch values for pions and protons, respectively. The long decay length allows to accept only Λ decays which have no match to a SDD track within $\pm3\sigma$ window. On the pair level, a p_T dependent opening angle cut $\vartheta_{p\pi^\pm}$ is applied. In addition, an Armenteros-Podolanski cut (36) with $q_T \leq 0.125$ GeV/c and $0.0 \leq \alpha \leq 0.65$ is applied in order to suppress background, admittedly with a considerable loss of signal. The α variable is a measure of the longitudinal momentum asymmetry, $\alpha = (q_L^+ - q_L^-)/(q_L^+ + q_L^-)$, where q_L^+ and q_L^- denote longitudinal momentum components of $\vec{p}^+$ and $\vec{p}^-$ calculated with respect to $\vec{p}_\Lambda = \vec{p}^+ + \vec{p}^-$. The q_T variable is the momentum component of $\vec{p}^+$ in the transverse plane perpendicular to $\vec{p}_\Lambda$. In the case of the $\bar{\Lambda}$ (K_S^0) particle one should exchange $\vec{p}_\Lambda$ with $\vec{p}_{\bar{\Lambda}}$ ($\vec{p}_{K_S^0}$) in the above definitions. Fig. 5 is the 2-dimensional $\alpha - q_T$ scatter plot which shows the signatures of Λ, $\bar{\Lambda}$ and K_S^0 reconstructed from the experimental data (37).

2.4.1. Λ

The combinatorial background is determined by rotating proton candidate tracks around the beam axis and constructing the invariant mass distribution. To decrease statistical errors in background assessment, ten rotations by random angles are performed.

The raw mass spectrum is shown in the left panel of Fig. 6. The pure Λ signal after subtraction of the combinatorial background shown at the right side has a non-Gaussian shape. This is owed to the facts that the observed mass and width depend on p_T and y and that the displaced secondary vertex is not used for recalculation of angles. The analysis is done separately in $p_T - y$ windows sufficiently small in size to keep the reconstructed Λ mass and width practically constant. The
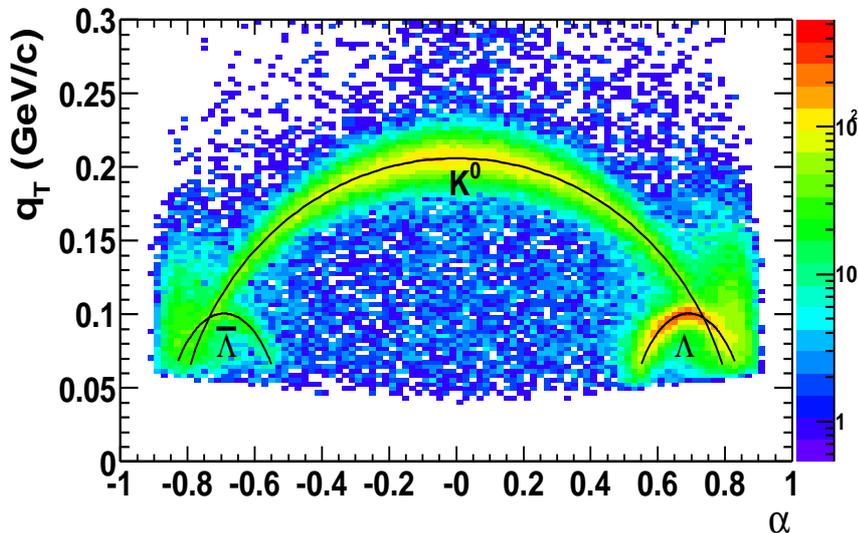
Figure 5: Armenteros-Podolanski plot shows *loci* of Λ, $\bar{\Lambda}$ and K_S^0 reconstructed from experimental data; taken from (37). See text.

signal distributions are fit by a Gaussian on constant background[1]. The mass of Λ particles strongly depends on p_T but practically not on rapidity, while the width depends on both (26). Once the mass and width are established for a given y and p_T both are kept constant for the rest of the analysis.

With these cuts, values of the signal-to-background ratio S/B and the significance $S/\sqrt{B}$ of about 0.04 and 500, respectively, are obtained. Here, S stands for the signal and B for the background. Both quantities strongly depend on p_T of the Λ. The largest values of $S/\sqrt{B}$ reside at $p_T \approx 1 - 1.5$ GeV/c with $y \approx 2$; this is the most populated area in the $y - p_T$ plane of the reconstructed Λ.

An example of reconstructed Λ in a given y-p_T-ϕ bin is shown in Fig. 7 (left). The yield of the Λ in a given bin is obtained by fitting the invariant mass distribution with a Gaussian. Plotting the yield versus ϕ for different p_T and y values one can construct the $dN_\Lambda/d\phi$ distribution (Fig. 7, right). Fitting these distributions with a function $c[1 + 2v_2' \cos(2\phi)]$, the observed elliptic flow values v_2' for different p_T and y were extracted. The obtained v_2' coefficients were corrected for the event plane resolution as described in Sect. 3.

2.4.2. K_S^0

The K_S^0 particles are reconstructed via the decay channel $K_S^0 \rightarrow \pi^+ + \pi^-$ with branching $BR = 68.95\%$ and decay length $c\tau = 2.68$ cm (35). In order to increase statistics, the dE/dx window is opened up to $\pm 2\,\sigma$ around the nominal Bethe-Bloch energy loss value for pions.
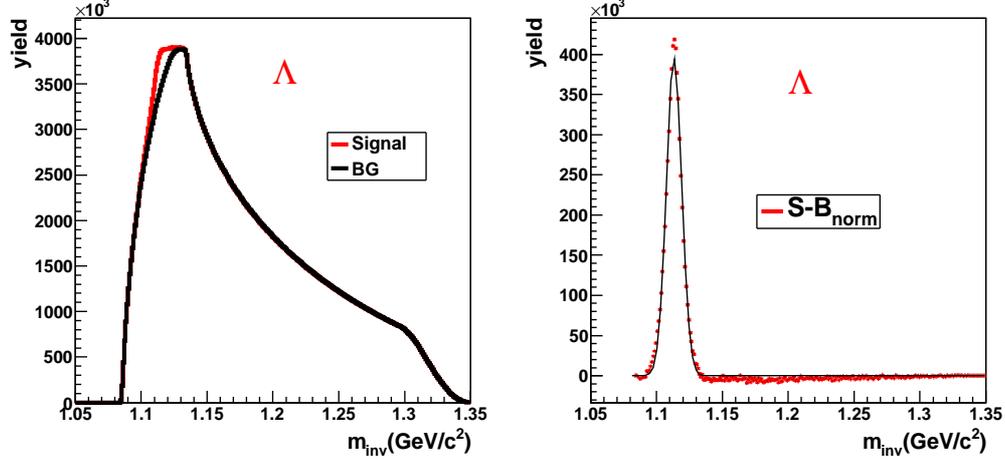
---

[1] found to be compatible with zero.

Figure 6: Left: A small enhancement of the signal is visible in the region of the Λ mass. Right: The invariant mass distribution of the Λ signal after subtraction of the normalized combinatorial background is significantly non-Gaussian.
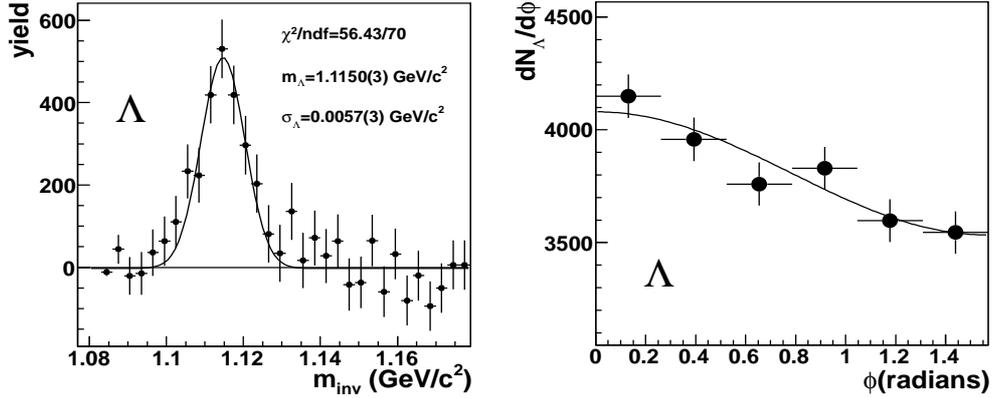

Figure 7: Left: Λ reconstructed for $1.62 \leq y \leq 1.69$ in rapidity, $0.675 \leq p_T \leq 0.8$ GeV/c in transverse momentum, and $15° \leq \phi \leq 30°$ in azimuth. Right: Elliptic flow pattern reconstructed from the Λ yield in ϕ bins for $p_T \approx 2.7$ GeV/c.

As the K_S^0 particle comes from the primary vertex, a possibility to suppress fake track combinations is given by a cut on the radial distance between the point where the back-extrapolated momentum vector of the K_S^0 candidate intersects the $x - y$ plane in the primary vertex. The numerical value of this cut is 0.02 cm. An opening-angle cut $\vartheta_{\pi^+\pi^-} > 50$ mrad is applied on pair candidates. Additionally, a cut on the z position of the secondary vertex ($z > 1$ cm) was applied. In order to suppress the contamination of Λ and $\bar{\Lambda}$ particles, an Armenteros-Podolanski cut with $q_T \geq 0.12$ GeV/c was applied (see Fig. 5).

For subtraction of the combinatorial background the mixed-event technique is used. To preserve the event topology, only events with similar multiplicity and orientation of the event plane are allowed for mixing. Windows are set to ±10% and ±22°, respectively. The event mixing is
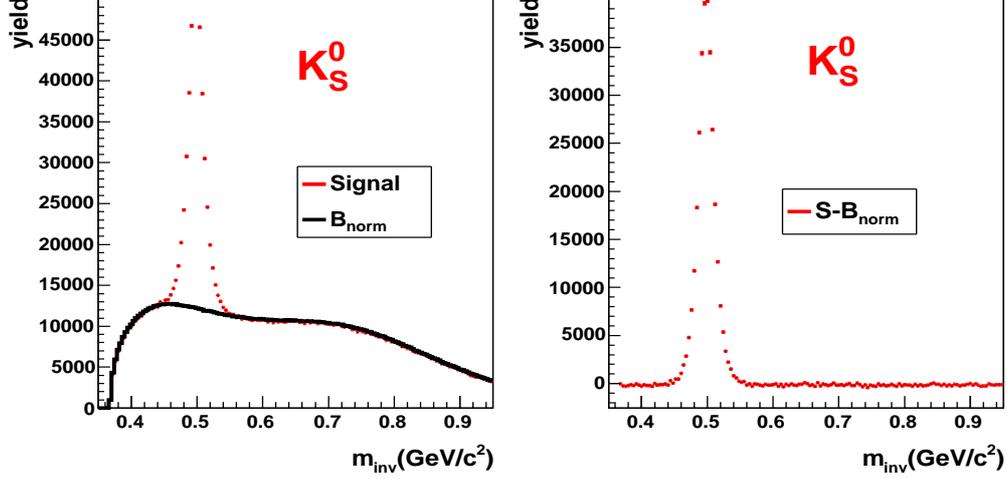
Figure 8: Left: The invariant mass distribution of the K_S^0 signal (red line) and the normalized combinatorial background (black line). Right: The invariant mass distribution of the K_S^0 signal after subtraction of the normalized background.

repeated 10 times.

The K_S^0 signal on normalized combinatorial background and after background subtraction is shown in Fig. 8. Mass and width of the reconstructed K_S^0 exhibit p_T and rapidity dependences. Values of S/B and $S/\sqrt{B}$ of ≈ 0.92 and 500 are obtained, respectively.
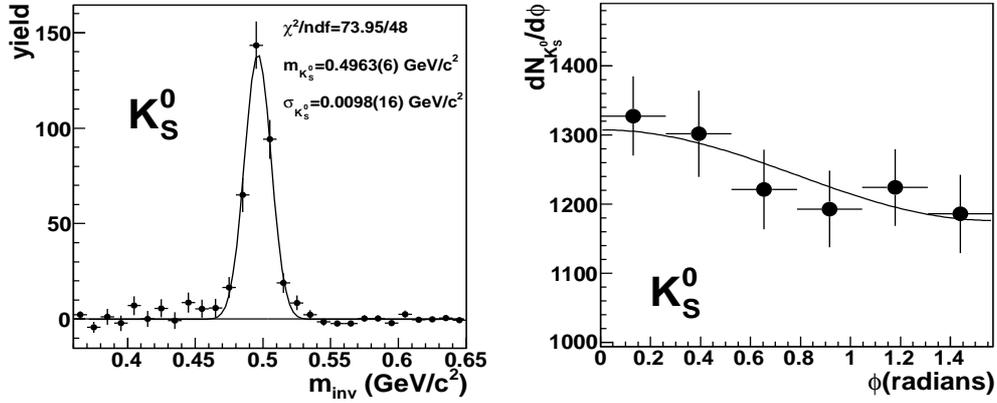

Figure 9: Left: K_S^0 reconstructed for $2.075 \leq y \leq 2.15$, $0.2 \leq p_T \leq 0.35$ GeV/c and $45° \leq \phi \leq 60°$. Right: Elliptic flow pattern reconstructed from the K_S^0 yield in ϕ bins for $p_T \approx 1.7$ GeV/c.

In Fig. 9 an example of K_S^0 reconstructed in a given y-p_T-ϕ bin (left) and a K_S^0 flow pattern (right) is shown. The evaluation of the elliptic flow magnitude is done in the same way as for the Λ particles.

3. Elliptic Flow Analysis

The flow analysis uses the event plane (EP) method, see e.g. (7, 8, 19, 26) and further references therein. We give here only a short outline to clarify notations. The elliptic flow parameter v_2 is the second term in the Fourier decomposition of azimuthal particle distributions in the plane transverse to the beam and with respect to the orientation of the reaction plane. However, the orientation of the reaction plane, being not known *a priori*, has to be reconstructed as 'event plane' (EP) for each event,

$$\frac{dN}{d(\phi_i - \Phi_{EP})} = A[\ 1 + 2v_2' \cos(2(\phi_i - \Phi_{EP}))\ ]. \tag{3}$$

Here, ϕ_i represents the azimuthal angles of outgoing particles. The anisotropy parameter v_2' is smaller than v_2 in magnitude due to the finite EP resolution.

The azimuthal acceptance was divided into 100 adjacent slices a, b, c, d, a, b, c, d, a, ... such that every fourth slice was assigned to a subevent a, b, c, or d, respectively. To avoid autocorrelations, particle tracks employed for reconstruction of the EP and of v_2' were taken from non-adjacent slices only.

Together with the reconstruction of the EP one calculates its resolution as the average difference $< \Phi_a - \Phi_b >$ between the EP's reconstructed from two subevents a, b. Its inverse is the correction factor $\mathcal{K}$ given by

$$\mathcal{K} = \langle 2\cos(2(\Phi_a - \Phi_b)) \rangle^{-1/2} \tag{4}$$

by which the measured second harmonic is upcorrected,

$$v_2 = \mathcal{K}\ v_2'. \tag{5}$$

As the EP resolution depends on multiplicity, $\mathcal{K}$ was calculated for different centralities. Fig. 10 shows for pion data the growing dispersion in EP orientation with multiplicity reflecting the fact that the decrease in anisotropy wins over the gain in statistics in deteriorating the resolution.
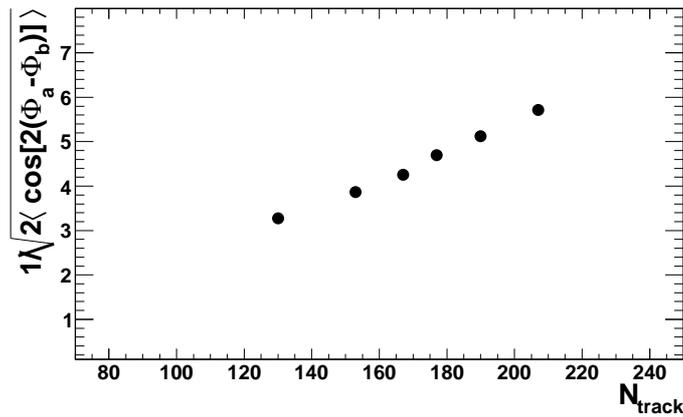

Figure 10: The correction factor *vs* TPC multiplicity for the 2-subevents method (pion data).
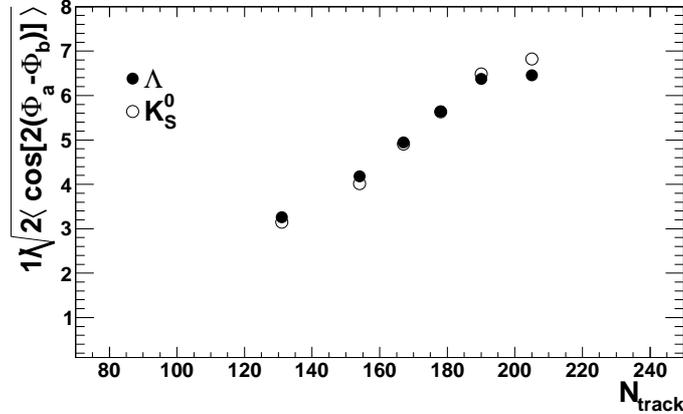
Figure 11: Correction factors *vs* TPC multiplicity for Λ (full circles) and K_S^0 (open circles) flow analysis.

To reduce autocorrelation effects, tracks chosen to be candidates for daughter particles were excluded from the determination of the event plane in case of Λ and K_S^0. The event plane resolution was calculated for each multiplicity bin separately. The correction factors $\mathcal{K}$ (Eq. 4), the inverse of the resolution, are plotted in Fig. 11 over TPC multiplicity for K_S^0 and Λ.

Due to instrumental inhomogeneities, the reconstructed event-plane density $< dN/d\Phi_{EP} >$ is not flat as it should be. In order to make it flat it is enough to apply successively first the method of recentering, and then the Fourier method of flattening (7).

3.1. Correcting for HBT effects

As we deal with a majority of charged pions, quantum effects among identical bosons give rise to space-momentum correlations of Hanbury-Brown and Twiss type (HBT): pions of the same charge tend to cluster in azimuth if their momentum difference $|\vec{p_1} - \vec{p_2}|$ is comparable to or below the uncertainty limit $\hbar/R$. The critical momentum difference, with a typical source radius $R \approx$ 5 fm, is about 40 MeV/c. Since the average pion momentum is much larger, the effect is of short range in azimuth. The HBT effect correlates pairs of low relative momentum; it is a positive correlation which fakes genuine flow.

In subtracting the HBT contributions to v_2 we followed Ref. (38) and used the source parameters (in the standard Bertsch-Pratt parametrization) obtained from CERES HBT data (39, 40). The correlation function has been modified to take into account the effects of the Coulomb repulsion (41). Several iterations of the correction procedure were necessary to stabilize on the final value of the integrated elliptic flow; the latter decreased thereby in relative size by $\approx 10\%$. The results are shown in the next section.

Concerning systematic uncertainties of the HBT correction, large relative corrections, and uncertainties are met with small magnitudes of flow at low p_T; and while v_2 quickly increases above 0.5 GeV/c, the corrections diminish in relative size even more rapidly and so the uncertainties. An error estimate is reached by an educated guess based on a former study (Ref.28) where errors in the source parameters have been included. The chaoticity parameter was given a large error margin of $\pm 50\%$ in view of unknown influences of long-lived resonances, the momentum resolution and of pairs in which one or both pions are not primaries or of rho-decay origin. This lead

to an estimate of the relative uncertainty in the correction of ±25%. The resulting relative errors in the HBT-corrected values amount to ±18% and ±13% at pT= 0.25 GeV/c and 0.325 GeV/c, respectively. At pT= 0.50 GeV/c, the systematic error is down to ±3%.

4. Postanalysis of Elliptic Flow of Candidate Pions

4.1. Overview

As illustrated in Sect.2.3, our dE/dx cuts do not effectively filter out kaons and protons. In order to purify the elliptic flow data of π^- candidates (denoted "π^-"), the knowledge of the K^- fraction as a function of p_T is required, but also of K^- differential elliptic flow. We sketch the recovery of negative-pion elliptic flow in Sect.4.2.

Positive pions are mixed with positive kaons and protons for $p \geq 1.2$ GeV/c. In order to isolate the *proton* elliptic flow from the measured v_2 data of π^+ candidates, $v_2^{"\pi^+"}$, we will use the particle ratios at 158 AGeV which recently became available from measurements of Pb+Pb collisions by the NA49 Collaboration (42).

The composition of the particle flux as accepted by the CERES spectrometer and filtered by the previous analysis cuts (26) has to be reconstructed. It is mandatory to properly simulate the effects of the pion-tuned dE/dx cut on kaons and protons. The dE/dx filter requires knowledge of particle momenta $p = p_T/\sin\vartheta$. Unfortunately, at the time this analysis was started, the information on polar angle ϑ from the doublet of Silicon-Drift Detectors was no longer accessible. Without it, the resulting spread in $\sin\vartheta$ over the acceptance, of almost a factor of two, would have blurred the dE/dx resolution. To avoid such degradation in quality, recourse was taken to a full Monte-Carlo (MC) simulation. We give details on the reconstruction of proton v_2 in Sect.4.3.

In a first approach to the acceptance correction we used analytic methods; although these calculations were made obsolete by the MC simulation, they serve as a valuable check on the final result. Besides, some are quite instructive and have been instrumental for preparing the input parameters of the MC simulations.

4.2. Processing elliptic flow of π^- candidates

The expression linking the π^- differential elliptic flow $v_2^{\pi^-}$ to the available data is

$$v_2^{\pi^-} = v_2^{"\pi^-"} + r_K^- (v_2^{"\pi^-"} - v_2^{K^-}). \tag{6}$$

Here, $v_2^{K^-}$ is the flow parameter of K^-, r_K^- denotes the particle ratio $r_K^- = N_{K^-}/N_{\pi^-}$. All quantities are functions of p_T. Statistical errors enter in a way that forbids to apply standard error propagation. Therefore, a simulation was performed treating the three experimental inputs as Gaussian random variables with widths equal to their statistical errors. For every channel of the p_T spectrum to be incremented, the flow parameter $v_2(p_T)^{\pi^-}$ is given by the average over many trials, its statistical error by the dispersion.

As input for $v_2^{K^-}$ we use the differential elliptic flow data for K_S^0 which will be presented in Sect.7. Because of the very similar mass and quark contents of kaons, a possible difference in v_2 can be considered small compared to the present accuracy (see below).

To improve on the statistical significance of the K_S^0 elliptic flow data, we have combined our results with those of NA49 (43, 44). The latter data have been collected at the top 13% of σ_{geo}. The two data sets are shown in Fig. 12 together with a 1-parameter fit according to $v_2(p_T) = A\, p_T^3 \exp(-p_T)$. The best fit resulted in $\chi^2/ndf = 0.44$. Shown is the best-fit curve for $A = 7.18 \cdot 10^{-2}$ in the centre, sandwiched between the $\pm 1\sigma$ statistical error bands of $\pm 17\%$ relative.

To quantify the unknown admixture of K^-, we have used the K^- and π^- transverse momentum spectra measured by the NA49 collaboration (42, 45). Details are given in the following section for the analogous case of positive-pion candidates. All steps and procedures, like centrality
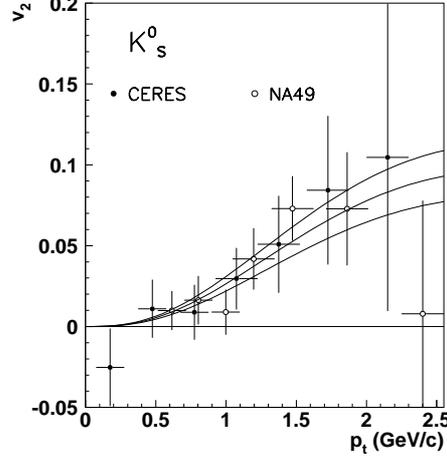
Figure 12: K_S^0 differential elliptic flow combining CERES data (this work; filled symbols) with NA49 data (ref.(43); open symbols). Centralities are (5.3 - 13)% of σ_{geo} for CERES (average 9.8%) and top 13% for NA49 data. The three lines show the best-fit within the 1-σ errors bands. Errors are statistical.

matching, dE/dx cut and acceptance corrections within the Monte-Carlo simulation, fully apply also to the negative-pion sample.

4.3. Processing elliptic flow of π^+ candidates

4.3.1. Outline

To determine the differential elliptic flow of the minor component of protons from measured $v_2(p_T)$ data of π^+ candidates, we make the simplifying assumption $v_2^{\pi^+} \approx v_2^{\pi^-}$, and use the differential flow of π^- derived in Sect.4.2 as substitute for $v_2(\pi^+)$ in the proton flow analysis below. For a discussion of possible violations of this assumption we refer to Sect.6.1.1 and for our assessment of related uncertainties to Sect.6.2.1.

The measured elliptic flow $v_2^{"\pi^+"}$ of the "π^+" candidate sample contains a contribution of proton elliptic flow v_2^p,

$$v_2^{"\pi^+"} = (N_{\pi^+}\, v_2^{\pi^-} + N_{K^+}\, v_2^{K^+} + N_p\, v_2^p)/(N_{\pi^+} + N_{K^+} + N_p). \tag{7}$$

More explicitly, the unknown magnitude v_2^p of the proton elliptic flow is derived as

$$v_2^p = ((1 + r_{K^+} + r_p)\, v_2^{"\pi^+"} - v_2^{\pi^-} - r_{K^+}\, v_2^{K^+})/r_p. \tag{8}$$

On the r.h.s., we substitute the measured $v_2(K_S^0)$ for $v_2(K^+)$. The only quantities yet unknown are the particle ratios $r_K^+ = N_{K^+}/N_{\pi^+}$ and $r_p = N_p/N_{\pi^+}$ specifying the contents of K^+ and protons in the "π^+" sample, respectively.

4.3.2. Differential particle yields

Invariant yields of charged pions, charged kaons and protons at midrapidity for inelastic Pb-Pb collisions at $\sqrt{s_{NN}} = 17.3$ GeV,

$$\frac{\mathrm{d}^2N(p_T)}{\mathrm{d}y\mathrm{d}p_T} = \frac{1}{2\pi p_T} \left. \frac{\mathrm{d}^2N}{\mathrm{d}y\mathrm{d}p_T} \right|_{y=0}, \tag{9}$$
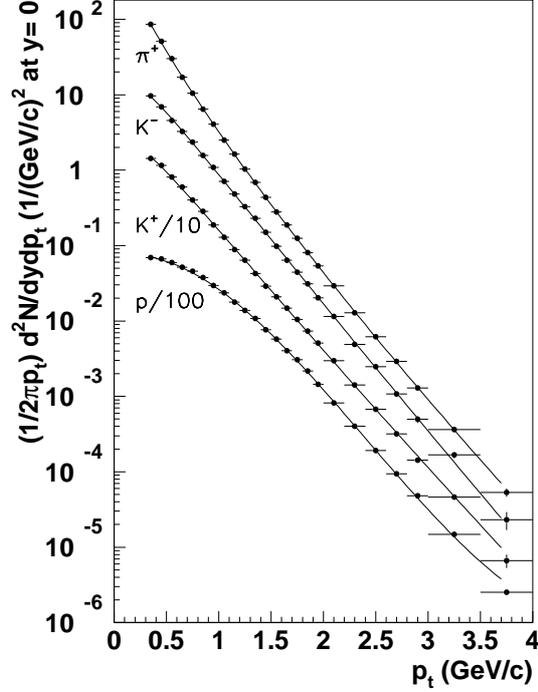
15

Figure 13: Invariant p_T-differential yields of π^+, K^+, K^- and protons from Ref. (42) with statistical errors, shown together with 3-parameter fits obtained by minimizing χ^2. K^+ data and curve are divided by 10, proton data by 100. The π^- spectrum, very close to that of π^+, is left out in order not to overload the figure.

which are relevant for the present study are those displayed in Fig. 8 of Ref. (42). The p_T spectra are adjusted to CERES centrality as described below. For the purpose of sampling p_T values at random which obey the proper density distributions, spectra are fit by 3-parameter exponential functions. The fits to the data are shown in Fig. 13. The authors of Ref. (42) have estimated the systematic errors, compounded from dE/dx, feed-down yields and acceptance corrections, as 2.2% for charged pions and K^-, 4.5% for K^+, and 3.7% for protons. The fits also shown in Fig. 13 deviate form the data points by typically less than 1%.

4.3.3. Matching Centralities

Our mid-central collision window (5.3-14.5)% of σ_{geo} does not find a close match among NA49 centrality classes. Since data for the closest (5-12.5)% selection were not available (46), we have used a linear combination of centrality classes (0-5)% and (12.5-23.5)%. By visual inspection of the NA49 p_T spectra for different centrality classes, a composition with equal weights seemed most appropriate. We also calculated the weighted means $\langle \sigma/\sigma_{geo} \rangle$ for the two slices representing the NA49 centrality classes 1 and 3 to determine the required composition quantitatively: the mixture of 55% of class-1 centrality (0-5)% combined with 45% of class-3 centrality (12.5-23.5)% well reproduces the mean centrality of 9.8% of CERES mid-central triggers and was used.
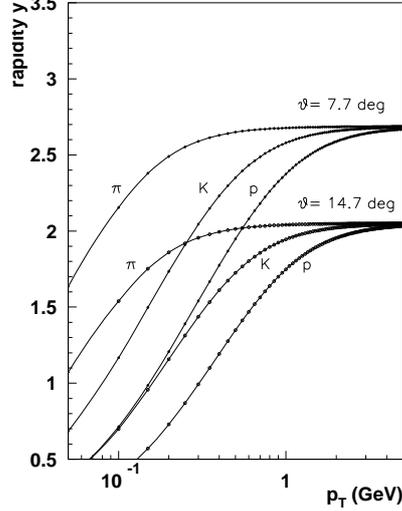
16

Figure 14: The boundaries of CERES acceptance defined by polar angles $\vartheta = 7.7°$ and $14.7°$ shift away from central rapidity ($y_{mid} = 2.91$) with decreasing p_T, the stronger the more massive the particle species, as shown here for pions, kaons, and protons. The η-acceptance $2.05 < \eta < 2.70$ coincides with y-acceptance at infinite momentum ($\beta = 1$).

4.3.4. Acceptance

CERES accepts a cone in polar angle of $7.7° < \vartheta < 14.7°$. The small acceptance in pseudo-rapidity, $\Delta\eta = 0.65$ units, spans the range $2.05 < \eta < 2.70$ and is close to midrapidity, $y_{mid} = 2.91$. For $p_T c$ smaller than particle mass mc^2, the acceptance is shifted down in rapidity with decreasing p_T as shown in Fig. 14.

The practicable assumption is made that the doubly-differential yields of Eq. 9 factorize in y and p_T. Particle yields within the CERES acceptance are then obtained by integrating the corresponding rapidity distributions between the p_T-dependent rapidity corners denoting the acceptance for given m and p_T, i.e. those shown in Fig. 14. We use the NA49 parametrization of the rapidity distributions by two identical Gaussians of width σ which are shifted from mid-rapidity by equal and opposite amounts $\pm y_S$ (47),

$$\frac{dN}{dy} = \mathcal{N}\left[exp(-\frac{(y - y_S)^2}{2\sigma^2}) + exp(-\frac{(y + y_S)^2}{2\sigma^2})\right]. \tag{10}$$

The values used in the present calculation for parameters $\mathcal{N}, \sigma$, and y_S are listed in Table 1. Those for charged pions and kaons were taken from Table III of Ref. (47). The yield parameter for π^+ was downscaled relative to that for π^- by the same factor by which both the total multiplicities and the values of $\langle dN/dy\rangle_{|y|<0.6}$ are observed to scale, by inspection of Table II of Ref. (47). For protons, the dN/dy parameters were determined by best-reproducing the distribution labeled CC2 in Fig. 6.6 of Ref. (48). This centrality class corresponds to (5-12.5)% of σ_{geo}, close to CERES centrality.

Particle invariant yields have to be averaged over the acceptance before taking ratios; those will no longer reflect yields at mid-rapidity alone, but will also depend on the shapes of the dN/dy distributions with appreciable differences among the particle species. In addition, the shift
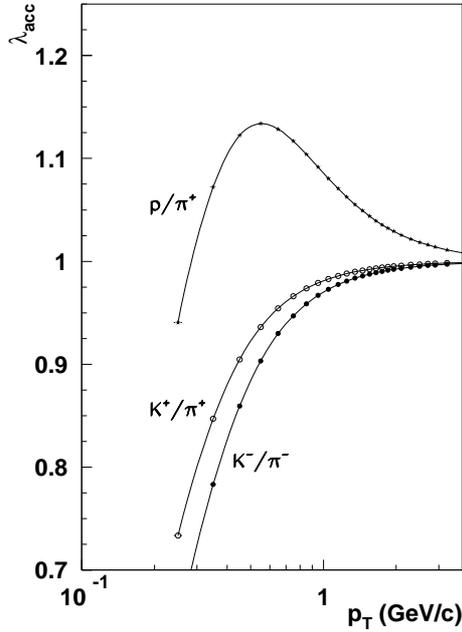
17

Figure 15: Acceptance correction functions λ_{acc} of Eq. 11 transforming NA49 particle ratios to CERES acceptance.

in rapidity is taken into account.

A suitable reference for the acceptance corrections of the invariant particle yields is the geometrical acceptance for massless particles ($\beta = 1$) for which pseudo-rapidity coincides with rapidity, $\eta \equiv y$; Fig. 14 would consist of two horizontal straight lines at $y = -0.86$ and at $y = -0.21^2$. With such reference, the acceptance correction is quantified by the ratio

$$\lambda_{acc}(p_T, m) = \left[\int_{y(\eta_{low};\, m, p_T)}^{y(\eta_{high};\, m, p_T)} \left(\frac{dN}{dy}\right) dy \right] \Big/ \left[\int_{y=\eta_{low}=-0.86}^{y=\eta_{high}=-0.21} \left(\frac{dN}{dy}\right) dy \right]. \tag{11}$$

---

^{2}we quote centre-of-mass rapidities downshifted from lab rapidities by the rapidity of the centre of mass in the lab, 2.91.

	π^-	π^+	K^-	K^+	p
$\mathcal{N}$	107.6±1.8	104.4±1.8	12.8±0.3	23.4±0.6	28.9±1.5
σ	1.18±0.02	same as π^-	0.81±0.02	0.88±0.04	1.01±0.02
y_S	0.72±0.02	same as π^-	0.727±0.010	0.839±0.012	1.41±0.012

Table 1: Parameters used to simulate dN/dy distributions using Eq. 10. From Ref. (47). See text.

18

The resulting correction functions are shown in Fig. 15 for the three particle ratios. The rapidity shift has opposite effects on the yield of protons and kaons: due to the rather compact distribution of kaons compared to the well-separated double humps in the dN/dy distribution of protons, the particle composition around 0.5 GeV/c is reduced by about 6% in kaons but enriched by 15% in protons over the $\beta = 1$ reference.

4.3.5. Monte-Carlo simulation

Transverse momenta for given particle type are generated from the respective probability densities, using standard methods (49). Before doing so, p_T spectra are adjusted to CERES centrality as described. 'Events' are filtered by conditions of acceptance and dE/dx cut. Once p_T is chosen, boundaries of the acceptance for the respective particle species are defined in rapidity, as shown in Fig. 14. Then y is chosen at random from the density distribution of Eq. 10 using the parameters of Table 1. Rapidity values outside the acceptance window result in rejection of the event. At this stage, the entire event is defined: the particle momentum p is calculated from m, p_T, and y, which also fixes the Bethe-Bloch most-probable dE/dx value. Gaussian noise is added to simulate the experimental resolution $\sigma = 0.10 \, dE/dx|_{BB}$. The historical filter set to (0.85-1.15)$dE/dx|_{BB}$ of *pions* during data analysis is activated. Now, the survival fractions of kaons and protons are determined as error integrals over the dE/dx distributions between the p_T-dependent boundaries of the cuts on charged pions. The p_T spectra are incremented by survival fractions f, $0 < f < 1$.

Monte-Carlo generated spectra require subsequent normalization to the experimental data after which they were modelled[3]. The NA49 particle yields are summed up from 0.30 GeV/c, the lower boundary of the first entry in the published spectra, to a reasonable upper boundary, i.e. to 4.0 GeV/c. The normalization is achieved by setting the initial MC-yield, prior to any filtering and summed-up over the said p_T range, equal to the sum over the respective data spectrum.

The p_T-integrated yield is multiplied by a factor x_S to transform the mid-rapidity yield to the yield averaged over acceptance,

$$x_S = \langle dN/dy \rangle_y^{\text{CERES}} / \, dN/dy|_{y=0} \,. \tag{12}$$

The transformation factors for particle ratios are listed in Table 2. Using identical binning, the statistical data errors are adopted.

---

[3]Since only particle *ratios* enter into Eq. 8, there is allowance for one free parameter common to all spectra.

particle ratio	K^+/π^+	K^-/π^-	p/π^+
x_S ratio	1.401 ±0.026	1.473 ±0.015	1.415 ±0.016

Table 2: Factors transforming MC-generated yield ratios at midrapidity to ratios of yields averaged over CERES' y-acceptance (Eq. 12). Errors are propagated from Table 1.

5. Elliptic flow of charged pions: Results

We present here the elliptic flow results of negative pions, illustrating the effect of the HBT correction and the subtraction of the K^- component as outlined in Sect. 3.1.

The elliptic flow of negative pion candidates is shown in Fig. 16 before and after the HBT correction. It is quite satisfactory to see that data start very close to zero and follow a quadratic p_T dependence for small p_T.
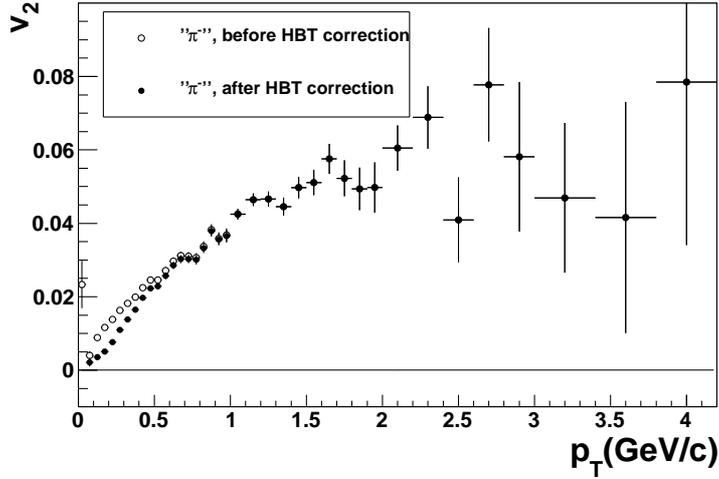

Figure 16: Elliptic flow $v_2(p_T)$ of π^- candidates before (open circles) and after (filled circles) correction for the HBT effect (mid-central trigger).

The p_T-differential elliptic flow $v_2(p_T)$ of negative pion candidates is displayed in Fig. 17, together with the $v_2(p_T)$ spectrum of negative pions obtained by subtracting the K^- component. Both spectra are corrected for HBT correlations as outlined in the previous section. Statistical errors are obtained by Monte-Carlo sampling along Eq. 6, treating all input data as Gaussian random variables. The estimate of 25% for the relative systematic error in the HBT correction amounts to about 15% of the corrected value around $p_T = 0.30$ GeV/c (for details see Sect. 3.1).

The K^- impurity is seen to have only a minor effect. The correction starts out positive, raises the v_2 value by about 0.005 at 0.6 GeV/c, decreases in size and changes sign at $p_T \approx 1.4$ GeV/c; it turns negative where v_2 of pions and kaons cross each other. The smallness of the correction follows from the rather small N_{K^-}/N_{π^-} ratio and the two elliptic flow parameters being close in magnitude.
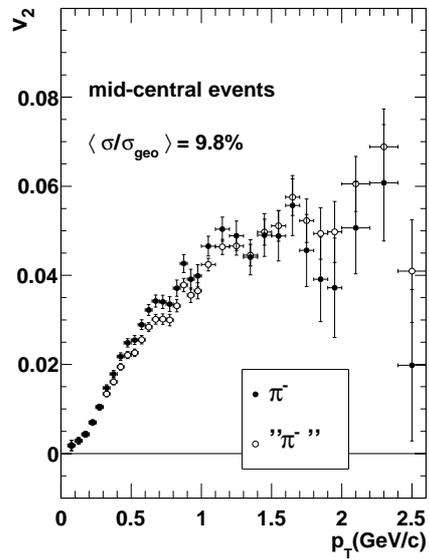
Figure 17: Differential elliptic flow $v_2(p_T)$ of negative pion candidates (open circles); and of negative pions after removing the K^- admixture (filled circles). The v_2 spectra are corrected for HBT correlations. Statistical errors are compounded from all sources entering Eq. 6 (mid-central triggers).

6. Elliptic flow of protons

6.1. Systematic uncertainties

Proton v_2 parameters in the present study are obtained as differences between two 'large numbers', the two pion flow measurements entering Eq. 8. Alarming as this might be in anticipation of relative errors getting out of control, the following evaluation will dispel such concern. A decisive advantage is that both measurements were performed and analyzed in identical settings.[4] In addition, CERES' full azimuthal coverage minimizes uncertainties in the EP determination and the flow measurement itself.

Other uncertainties common to pions of both charges are related to the centrality determination, and the dE/dx and acceptance cuts. Summing up the individual error estimates in quadrature yields 6%. A 'common-mode' error of this size is applied to both pion flow parameters and the response is calculated for the full p_T range of interest. The deviations in proton v_2 rise from negligible levels with increasing p_T to $\Delta v_2 \approx 0.008$ at 2.5 GeV/c.

Uncertainties linked to HBT correlations and the corrective measures taken are common to both pion flows and treated as *relative* errors. The HBT correction is largest at the lowest p_T bin of 0.325 GeV/c. A systematic relative uncertainty of 15% in the corrected values at $p_T \approx 0.30$ GeV/c causes an uncertainty in proton flow of $\Delta v_2 \leq 0.004$ which decreases quickly with rising p_T to practically vanish around 0.6 GeV/c. The directly identified protons (the four asterisk points in Fig. 19 below) are free of HBT correlations and related uncertainties.

One may think also of uncertainties in only one of the two pion flow parameters which remain unbalanced. The subtraction of the K^- component from the "π^-" candidate flow parameter is the only such example we are aware of. An estimated relative error of 8% in v_2 of K^- combined with a 5% relative uncertainty in the K^-/π^- particle ratio has little impact.

We have not corrected the pion elliptic flow data for non-flow correlations apart from HBT. Autocorrelation effects of short range between the samples used for flow measurement and for determining the event plane, respectively, were avoided by accepting only non-contiguous combinations. In the proton flow analysis we may assume that on average non-flow correlations in the positive and the negative pion samples cancel each other; for the remaining proton elliptic flow we argue that jet-like correlations, the main physics source of non-flow correlations for pions, have negligible proton content at this energy.

So much to systematic uncertainties in CERES data. The MC simulation introduces additional uncertainties. Errors in particle ratios have been derived from dn/dp_T spectra of Ref.(42) as 5.0% for K^+/π^+, and 4.3% for p^+/π^+. The MC-generated spectra carry small normalization errors, quoted in Table 2. Further errors arise by simulating dE/dx cuts and acceptance corrections, to our estimate of 3% each; they add up to 6.8% and 6.1% for the $K^+/\pi+$ and $p/\pi+$ ratios, respectively. The calculated uncertainties induced in proton v_2 are largest at low p_T but remain below 0.003. More harmful is the relative uncertainty in v_2 of K_S^0: although deviations in proton v_2 start well below 0.001, they approach 0.008 at the largest p_T.

6.1.1. A digression: pion flow asymmetry

Our derivation of proton $v_2(p_T)$ rested on the plausible assumption that $v_2(\pi^+)$ and $v_2(\pi^-)$ are sufficiently close. With recent dicussions of exciting new physics related to chiral magnetic

---

[4]An exception is the different sign of track curvature in the TPC. The zero-deflection was fine-tuned by reconstructing the same mass for Λ and $\bar{\Lambda}$ (32).

effects (50), an asymmetry in elliptic flow of particles and antiparticles has come into focus and its observation was recently reported by the STAR Collaboration (30). Preliminary data for minimum-bias Au+Au collisions at $\sqrt{s_{NN}}$= 7.7 and 11.5 GeV show sizeable asymmetries[5]

$$\mathcal{A} = (v_2(\pi^-) - v_2(\pi^+))/v_2(\pi^+) \tag{13}$$

at very low p_T.[6]

There are reasons to assume the pion flow asymmetries will be considerably reduced towards more central collisions. We will go along some of the arguments that have been suggested, mostly by the authors of Refs. (50, 30) with emphasis on the expected p_T and centrality dependence. We start with the more conventional scenarios.

Resonance decays have been discussed for effects on pion elliptic flow (51) and possible violations of the naive quark coalescence model (52). Other than ρ-mesons, $\Delta(1232)$-resonances may induce charge-dependent effects in flow by two reasons: (i) the isospin asymmetry between u and d flavours[7] gives an edge to excitation of Δ° and Δ^- over Δ^+ and Δ^{++}, causing a surplus of π^- over π^+ decays. (ii) As Δ's are likely to be recombined from two hadrons ($N\pi$), their v_2 will increase over strict number-of-constituent-quark (NCQ) scaling, and decay pions are to show *larger* v_2 than directly produced pions (51, 53). Since Δ-decay pions are very soft, the flow asymmetry should show at very low p_T.

The asymmetry is transmitted only by decay pions which leave the fireball without being rescattered prior to thermal freeze-out. The condition is met by only a small fraction of Δ's decaying close to thermal freeze-out.[8] The number of unscathed decay pions should be rather independent of centrality: production of Δ's grows with N_{ch} as do rescattering losses due to increased density. However, the asymmetry in the pion sample for more central collisions is reduced by an increasing share of thermal pions ($\propto N_{ch}$). At the bottom line, $\mathcal{A}$ induced by resonance decays should scale inversely with $< N_{ch} >$. For our 10% trigger we estimate a drop to about 40% relative to the (0-80)% minimum-bias trigger of the STAR data.

Another scheme for violation of NCQ scaling has been proposed (55) in which partons carry larger amounts of flow strength arriving at midrapidity from stopped baryons, than those from $q\bar{q}$ pairs. This effect yields the correct sign, but is rather smallish: at $\sqrt{s_{NN}}$= 8.86 GeV, the asymmetry is about 1%. At 17.3 GeV, it is further reduced by a factor 2.6[9]. In this model, the fraction of constituent u quarks transported by baryon stopping decreases from 0.50 to 0.24 between 8.86 GeV and 17.3 GeV, respectively.[10] This suggests an equal reduction in proton density at midrapidity and hence of Coulomb repulsion of positive pions as a possible cause of the asymmetry, whatever its importance might be.

The Chiral Magnetic Effect (CME): a transient magnetic field induces an electric current at finite baryo-chemical potential in presence of a chiral asymmetry between left- and right-handed quarks. The current generates an electric quadrupole with positively charged poles 'above' and 'below' the reaction plane causing the asymmetry $v_2(\pi^-) > v_2(\pi^+)$ (50). The numerical estimates of (50) are by and large consistent with the preliminary data (30). It is seen from Ref.(56) that

---

[5]we changed the sign so that $\mathcal{A} > 0$ in accord with the STAR results.

[6]we read from the J. Phys. paper (30), Fig. 2 (top right) $\mathcal{A}$ values for $\sqrt{s_{NN}}$= 7.7, 11.5, and 39 GeV and p_T= 0.3 GeV of 30%, 26%, and 10%, respectively, which at p_T= 0.5 GeV, reduce to to 11%, 8%, and 4%; minimum-bias trigger.

[7]the neutron-to-proton ratio for Pb-Au is 1.52.

[8]reduction of resonance yields relative to stable particles was described recently (54).

[9]using the parameters of Ref. (55) and particle data from NA49 at 17.3 GeV.
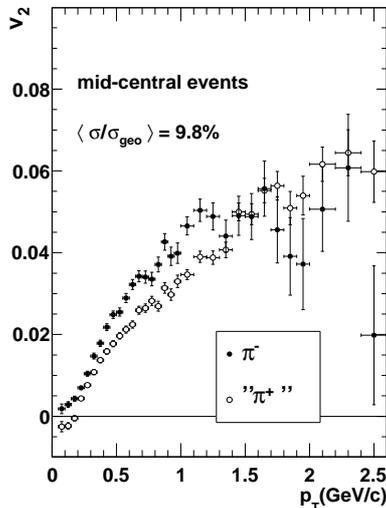
[10]quoting values of X_T defined in Ref.(55).

Figure 18: Differential elliptic flow $v_2(p_T)$ of π^+ candidates (open circles) and of identified negative pions (filled circles) shown already in Fig. 17. The two flow spectra differ by the K^+ and proton admixtures to the former, open-circled spectrum. A possible pion-flow asymmetry has been neglected.

observables which measure the correlation of positive/negative charges to the reaction plane (57) are reduced by one order of magnitude between semi-peripheral collisions of 50-60% centrality and mid-central collisions below 20% of the geometrical cross section.[11] It is plausible to assume that a CME-inflicted pion flow asymmetry is reduced also by one order of magnitude at our 10% centrality, compared to the minimum bias results.

In summary, Δ-resonance decays and the CME seem plausible candidates for inducing an isospin asymmetry on pion flow at low p_T, of the correct sign and possibly of the magnitude indicated by the preliminary STAR data (30). The arguments presented suggest that $\mathcal{A}$ is considerably reduced in more central collisions compared to minimum-bias collisions studied by STAR.

6.2. Results

The primary data entering the proton flow analysis are displayed in Fig. 18. The indication of a negative excursion in v_2 of the "π^+" candidates at low p_T, absent in π^- flow, gave the incentive for the present reanalysis. The derivation of proton $v_2(p_T)$ is performed by Monte-Carlo simulation of Eq. 8 using our $v_2(p_T)$ data for K_S^0 and p_T spectra of charged hadrons from the NA49 Collaboration. The simulation serves to adapt the NA49-based particle ratios to CERES conditions and not to introduce any model assumptions.

The resulting proton $v_2(p_T)$ spectrum between 0.30 GeV/c and 2.60 GeV/c is displayed in Fig. 19. It extends over the range where data both of particle spectra and kaon flow were available. At lower p_T, four additional points of directly identified protons[12] are shown by asterisks.

---

[11] referring to the plot of a_{++}, a_{--} vs centrality in Fig. 3 of Ref.(56).
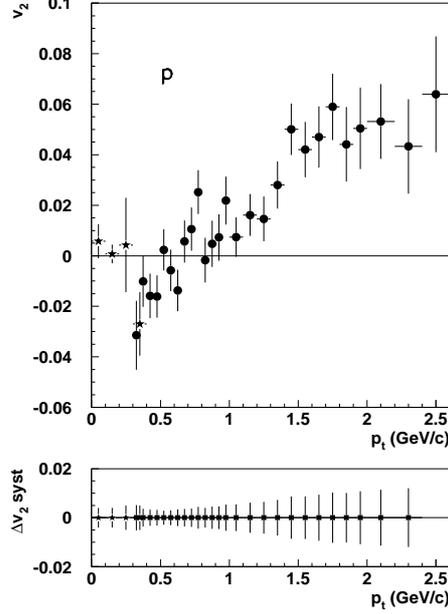
[12] see dE/dx plot Fig. 4 in Sect. 2.3.

Figure 19: Proton $v_2(p_T)$ (upper panel, filled circles) reconstructed from the "π^+" candidate sample. The first four points apply to protons directly identified by dE/dx (solid asterisks). Statistical errors derive from CERES v_2("π^+") and $v_2(K_S^0)$ data, and NA49 particle spectra, by Monte-Carlo sampling. Mid-central events, (5.3-14.5)% of σ_{geo}, weighted average 9.8%. Lower panel: Systematic errors applicable to data points in upper panel, plotted to scale; see Sect. 6.1.

The first three of these data points, from $p_T = 0.05$ GeV/c upward, are compatible with $v_2 = 0$, the fourth seems to bridge to the reconstructed points in an apparently abrupt downward swing. Considering the large statistical errors, the sawtooth impression may be misleading. The excursion at low transverse momenta of proton elliptic flow magnitudes below zero takes its minimum close to 0.4 GeV/c with $v_2 = -0.0290 \pm 0.0092$, 3.2σ below zero.[13]

The systematic errors estimated in Sect. 6.1 are displayed in the bottom panel of Fig. 19. The uncertainties due to the pion flow asymmetry are quantified in the following section 6.2.1.

6.2.1. Setting an upper bound on the flow asymmetry

An asymmetry in pion elliptic flow threatens to falsify the results on proton elliptic flow we derived under the assumption that v_2's are equal for π^+ and π^-. Moreover, the subtraction of $v_2(\pi^-)$ in place of the smaller $v_2(\pi^+)$ in Eq. 8 would be an overcorrection that might have caused the peculiarity of the proton flow data, i.e. its turn to negative values at small p_T.

A meaningful *upper bound* on the asymmetry, however, is obtained from the proton v_2 data: the lowest of the reconstructed points at $p_T = 0.325$ GeV/c is close to the v_2 point of directly identified protons at $p_T = 0.35$ GeV/c, marked by an asterisk in Fig. 19; being independent of the asymmetry issue, it serves as reference point. By tuning the asymmetry parameter in the Monte-Carlo simulation such as to move the reconstructed point by one standard deviation *above* the

---

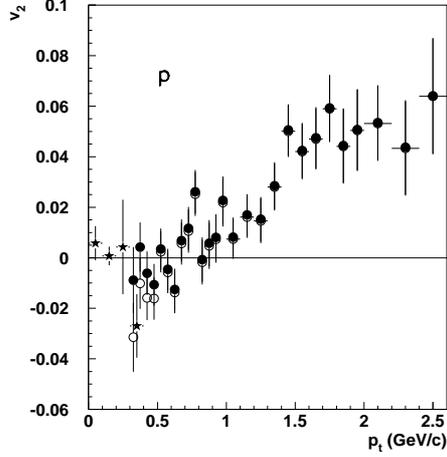[13]weighted mean of fourth direct and first reconstructed data point in Fig. 19

Figure 20: Monte-Carlo simulation of proton v_2 fixing the asymmetry in pion flow $\mathcal{A}$ at 8.6% at p_T= 0.325 GeV/c such that v_2(0.325) (the first of the full-circle points) deviates by one σ from the directly identified point at 0.35 GeV/c (the last of the four asterisk points). At higher p_T, the $\mathcal{A}$ values are made to decrease rapidly, modelling the strong p_T dependence of the preliminary STAR data (full circles). The proton v_2 data of Fig. 19 based on $\mathcal{A}$= 0 are shown by open circles. See text.

reference point,[14] an *upper bound* $\mathcal{A}_{max}$(0.325)= 8.6% is obtained. To proceed further, we turn to the STAR data which show a dramatic decrease of $\mathcal{A}$ with p_T, between 0.3 and 0.5 GeV/c by a factor of ≈ 3 (see footnote on p. 24). We use this p_T dependence to extend our upper bound of asymmetry-related uncertainties beyond the calibration point: in the simulation shown in Fig. 20, $\mathcal{A}$ is taken to decrease linearly to 0.7% at p_T= 0.525 GeV/c and stay constant above. We like these calculations be understood as defining the systematic errors of the proton $v_2(p_T)$ data with respect to the pion-flow asymmetry issue.

If the asymmetry were caused by Δ decays, the STAR data scaled to our centrality would come very close to our bound; and the strong p_T dependence would be understood. If caused by CME, the scaled $\mathcal{A}$ would be much smaller than our upper bound.

---

[14] speaking about the *rms* of the combined data point errors

6.2.2. The rapidity window for proton flow

Fig. 21 demonstrates that protons for which the elliptic flow data $v_2(p_T)$ has been derived originate from about 1.2 units below midrapidity. This reflects the rapidity shift of the acceptance for low-p_T protons while the η acceptance of CERES can be recognized in the π^+ distribution (reduced five fold).
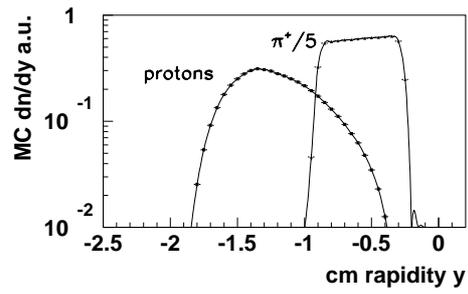

Figure 21: dN/dy of protons and π^+, in log scale. Monte-Carlo simulation.

7. Elliptic flow of Λ and K_S^0 particles

7.1. Results

The upper part of Fig. 22 shows the differential flow data for K_S^0. Statistical errors are large, mostly due to the strong cut on the secondary vertex position during reconstruction. We show here the CERES data alone and refer to a comparison of the combined CERES and NA49 data with hydrodynamical calculations to Sect. 8.

Absolute systematic errors in v_2 of K_S^0, estimated by varying the cut on the z position of the secondary vertex, are $^{+0.000}_{-0.002}$ for $p_T < 1.25$ GeV/c and $^{+0.00}_{-0.03}$ for $p_T > 1.25$ GeV/c. Systematic errors are quadratically small compared to statistical errors.

The Λ elliptic flow displayed in the lower part of Fig. 22 shows a p_T dependence characteristic for baryon elliptic flow. In the region of small p_T, the magnitude of v_2 is small but steadily increases with p_T. At $p_T \approx 1.7$ GeV/c, v_2 exceeds 5% and rises further. The absolute systematic error Δv_2 is estimated from two different ways of Λ reconstruction with emphasis either on the size of the signal S, or on the signal-to-background ratio S/B; it is $^{+0.001}_{-0.007}$ for $p_T < 1.6$ GeV/c and $^{+0.00}_{-0.02}$ for $p_T > 1.6$ GeV/c which is again small compared to the statistical errors.

For both species, K_S^0 and Λ, the lowest v_2 value at $p_T = 0.175$ GeV/c and 0.55 GeV/c, respectively, lies by about $1\,\sigma$ below zero.

7.2. Comparison to NA49 and STAR experiments

A comparison to results from NA49 (44) at the same energy ($\sqrt{s_{NN}} = 17.3$ GeV) and to STAR results (58) at $\sqrt{s_{NN}} = 200$ Ge is shown in Fig. 23. The NA49 and CERES data are in reasonably good agreement. In order to compare STAR to CERES results, the former have been rescaled to the centrality used in the CERES experiment. The appropriate factor is obtained by plotting the STAR v_2 values vs centrality for different transverse momenta of Λ and K_S^0 particles. After rescaling, the STAR the v_2 values measured at the RHIC energy are $15 - 20\%$ higher due to the higher beam energy.
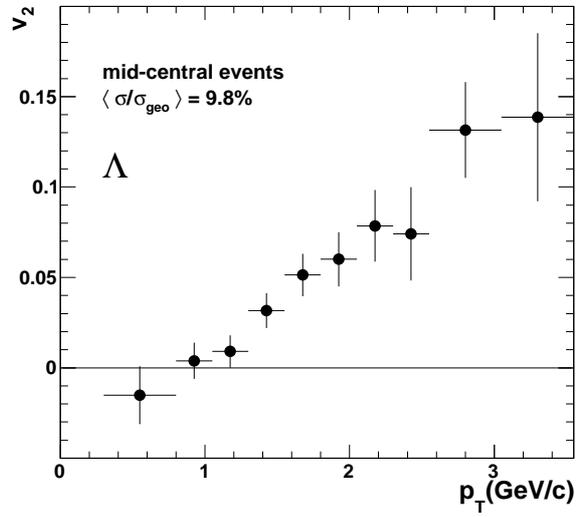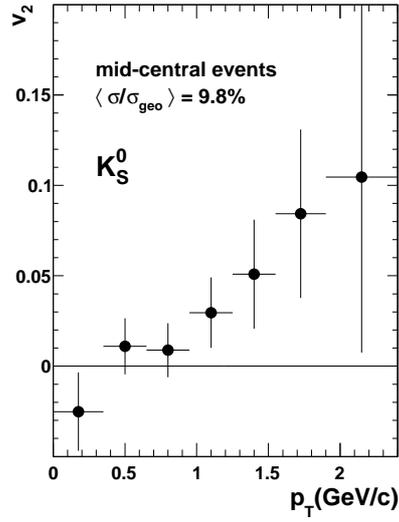
Figure 22: Differential elliptic flow $v_2(p_T)$ of reconstructed K_S^0 mesons (top) and Λ hyperons (bottom). Mid-central collisions. Errors are purely statistical.
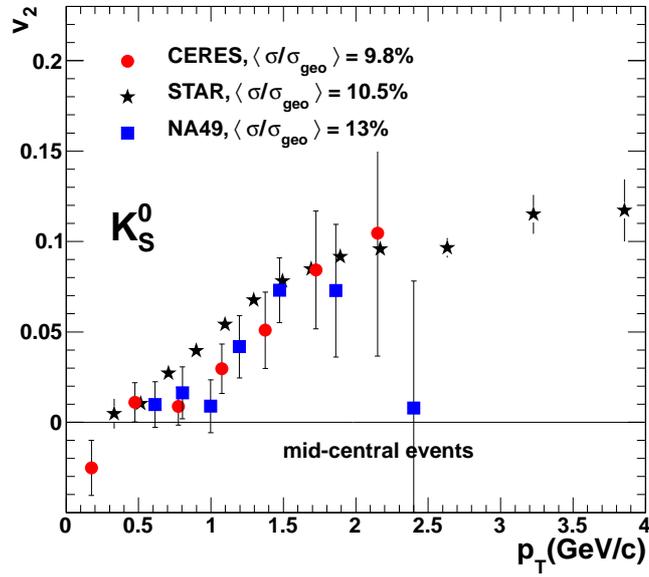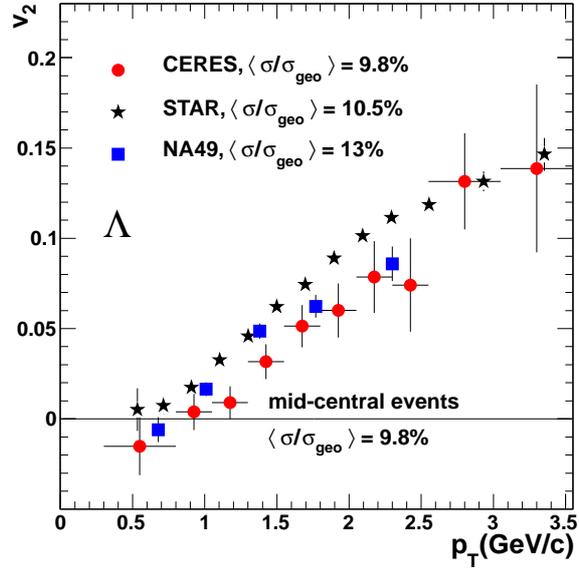
Figure 23: Comparison of Λ (top) and K_S^0 (bottom) elliptic flow data of CERES to measurements of NA49, Ref. (44), and STAR, Ref. (58).
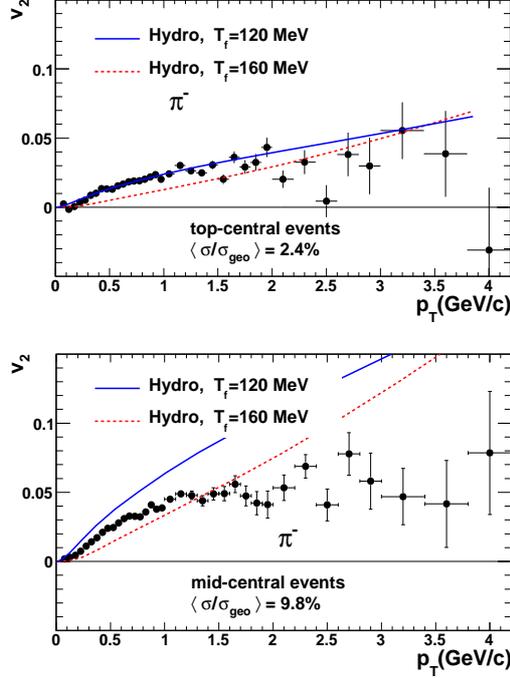
Figure 24: Pion differential elliptic flow compared to ideal hydrodynamics calculations (19, 59) for two kinetic freeze-out temperatures, T_f = 120 MeV (blue solid) and T_f = 160 MeV (red dashed). Top: top-central collisions, Bottom: mid-central collisions. Data are not corrected for K^- admixture. Statistical errors.

8. Comparison to ideal hydrodynamics calculations

8.1. Overview

We compare the results to ideal-hydrodynamics calculations by P. Huovinen (19, 59). These are performed in 2+1 dimensions assuming boost-invariant longitudinal flow. Initial conditions are fixed by reproducing the p_T spectra of negatively charged particles and protons in Pb+Pb collisions at top SPS energy. Assumed is a first order phase transition to quark gluon plasma at a critical temperature of T_c = 165 MeV. The calculations were done for two choices of kinetic freeze-out temperature[15], T_f = 120 MeV and T_f = 160 MeV.

Kinetic freeze-out at T_f = 160 MeV may be a handy way to shorten the evolution of the hadronic fireball and reduce v_2 thereby, but it fails in describing the proton p_T spectra which come out too steep due to insufficient radial flow, as noticed some time ago (19). However, by comparing the data to alternative freeze-out conditions, we may find out how much the elliptic flow gains in magnitude during the hadronic fireball evolution, or even looses.

8.2. π^- elliptic flow

The top-central data appear to be in perfect agreement for 'standard' T_f = 120 MeV, as shown in the upper part of Fig. 24 [16]. However, it is hard to rule out, or it may even be likely, that the

---

[15]also known as decoupling temperature T_{dec}

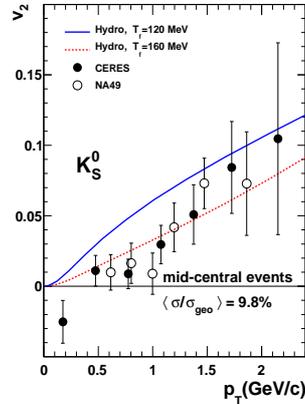[16]for easy comparison figures in Sect. 8 are plotted to the same scale in v_2 and in p_T.

Figure 25: K_S^0 elliptic flow data from Fig. 12 compared to ideal hydrodynamics calculations for T_f= 120 MeV (blue solid line) and T_f= 160 MeV (red dashed line).

good agreement occurs by accidental cancellation between fluctuations that raise v_2 and flow-damping effects reducing it. For mid-central collisions, the data seem to prefer a position in between the two hydro curves till about 1.0 GeV/c and then saturate, whereas the hydro curves continue to rise about linearly with p_T, see Fig. 24, bottom. Note, that until about 1.2 GeV/c, the mid-central pion flow data remain significantly *above* the $T_f = 160$ MeV curve as to be expected.

This is at variance with earlier CERES differential flow data taken with more peripheral triggers (σ/σ_{geo}= 13% - 26%) (19). These elliptic flow data for h^- and identified $\pi^\pm$, the latter with p_T threshold at 1.2 GeV/c, stay below the predictions for $T_f = 120$ MeV, but fall right on top of the $T_f = 160$ MeV line[17]. In fact, the two CERES data sets seem to confirm that departures from ideal hydrodynamics increase with increasing impact parameter of the collision.

Similar conflicts with ideal hydrodynamics have also been reported from RHIC experiments (58, 60). Whether this indicates incomplete thermalization during primary stages (23, 61), or increasing viscous corrections (24, 29), or a mixture of both, remains to be seen.

8.3. K_S^0 elliptic flow

The CERES/NA49 combined elliptic flow data for K_S^0 are compared in Fig 25 to ideal hydrodynamics calculations. Surprisingly, for $p_T \leq 1.1$ GeV/c data points tend to fall *below* the $T_f = 160$ MeV line.

8.4. Proton elliptic flow

The proton elliptic flow $v_2(p_T)$ data are shown again in Fig. 26 for comparison with hydrodynamics calculations. With standard freeze-out temperature, the calculation overpredicts the data as in the pion case. What appeared to be a tendency for K_S^0 is for proton $v_2(p_T)$ plain fact: the majority of data points resides *below* the T_f= 160 MeV line. With decreasing p_T, the ideal-hydro curve bends smoothly towards zero while the data continue to fall about linearly until about 0.2 GeV/c. For such early freeze-out, as implied by the large T_f, it is hard to attribute

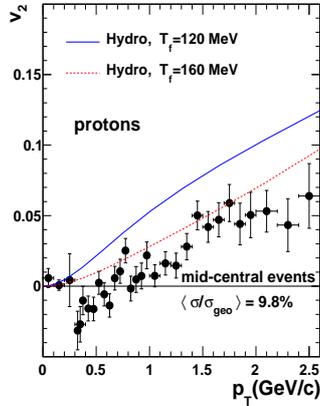---

[17]referring to Fig. 1c in (19).

Figure 26: Proton $v_2(p_T)$ data of Fig. 19 compared to ideal hydrodynamics predictions for two freeze-out temperatures (see Fig. 24).

the v_2 reduction to a decreased contribution from hadronic interactions. The observation rather seems to suggest that a suppression mechanism or dissipation is at work which is not present in the ideal-hydro calculation.

To what extent negative v_2 values are reached is surely a matter of the asymmetry value; for our upper-bound $\mathcal{A}$, all negative v_2's with one exception remain negative. But more important, the perception that v_2 data for protons towards low p_T fall further below and away from the 160 MeV-ideal hydro curve as in the case of K_S^0 remains fully valid. The theory seems to miss some basic ingredient, at least in the present modelling, to account for the marked reduction in v_2 at low p_T already indicated for K_S^0.

8.5. Λ elliptic flow

The reduction in v_2 is seen in Fig. 27 to persist for Λ elliptic flow. The Λ results could be termed 'perfectly in line' with previous findings, would that not be an overstatement in view of the large statistical errors and the sparse low-p_T data in case of the Λ. Even an excursion into negative v_2 values as seen for protons would fit into the Λ flow data at very low p_T.

The data suggest that deviations from ideal hydrodynamics grow with particle mass. That in fact the deviations seen in Λ flow are not stronger than those in proton flow may well be due to the small lever arm: the relative gain from $m(p)$ to $m(\Lambda)$ is only 19%, compared to the steps $m(\pi)$ to $m(K)$ (250%), and $m(K)$ to $m(p)$ (90%); and to limited data precision.
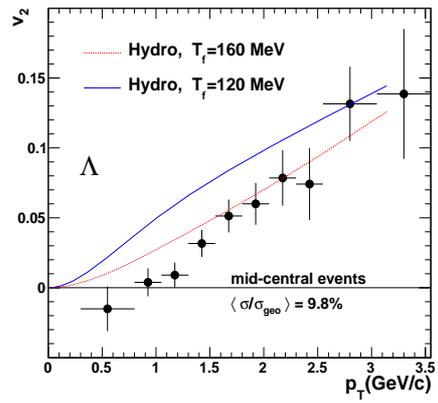
33

Figure 27: Λ elliptic flow data and predictions of ideal hydrodynamics for $T_f = 120$ MeV (blue solid) and $T_f = 160$ MeV (red dashed). Mid-central events. Errors purely statistical.

9. Discussion and Conclusion

We have presented differential elliptic flow measurements $v_2(p_T)$ at $\sqrt{s_{NN}} =$ 17.3 GeV of K_S^0 and Λ in mid-central collisions, supplemented by $v_2(p_T)$ of negative pions. We presented also differential elliptic flow $v_2(p_T)$ of protons, at low p_T by direct identification, for $p_T \geq$ 0.35 GeV/c by reconstruction from impure positive-pion samples. The synopsis of differential elliptic flow spectra from π to K_S^0 to p and Λ in comparison with calculations of ideal hydrodynamics discloses a marked decrease of v_2 values towards low p_T, getting stronger the larger the hadron masses. That negative values are reached in proton v_2 maybe seen as the most prominent feature of this trend.

These results were shown to be robust with respect to isospin asymmetries in elliptic flow of charged pions as reported recently by STAR at RHIC (30) for minimum-bias $Au + Au$ collisions. An upper limit on $\mathcal{A}$ could be derived by using our direct proton point for reference, at the lowest p_T measured where $\mathcal{A}$ is supposedly largest.

Indications of negative-valued elliptic flow of heavy particles from SPS and RHIC experiments at low p_T and central to mid-central collisions have been reported (62, 63, 64), but differential flow data at SPS or RHIC energies — with more than one or two points below zero — have to our knowledge not been presented before. A tendency of massive particles towards negative v_2 values at low p_T is ascribed to the conjunction of elliptic flow and strong radial expansion under specific freeze-out conditions. The authors of Ref. (21) like to illustrate and quantify these phenomena using a 'blast-wave' description (65) which is based on an interplay of transverse flow, imparting a momentum gain proportional to particle mass, and elliptic flow anisotropy which renders such momentum shift larger in-plane then out-of plane. The particle density at low p_T is depleted in-plane more than out-of plane, and elliptic flow values tend to become negative. The depletion mechanism works best for steep p_T spectra, i.e. those with low inverse slopes or temperature.

In a recent hydrodynamic study (29) a large hadronic shear viscosity-to-entropy ratio was implemented to calculate p_T spectra and differential elliptic flow of hadrons produced in 200 AGeV Au+Au collisions. While viscosity in the late hadronic phase suppresses elliptic flow in general, the consequences are striking for protons: for $\eta/s > 0.42$ and $T_f \leq$ 120 MeV, proton v_2 turns negative at small p_T and the similarity to our data can hardly be overseen[18]. The authors stress that this effect is entirely owed to viscous corrections δf (24) creating large average transverse pressure. The viscous mechanism, growing with m_T, appears to initiate a kind of blast wave with the potential to produce effects very similar to those we observe in proton elliptic flow.

Some caution is advised. An earlier but related viscous hydrodynamics study (66) remained inconclusive as proton spectra and charged hadron elliptic flow were found to have non-compatible requirements on the size of (constant) η/s. Besides, Ref.(67) points to possible consequences of yet unresolved ambiguities in viscous hydrodynamic calculations for identified particle observables.

We hope that our results are useful to better understand the role of shear viscosity during the late hadronic stages that terminate heavy-ion collisions at all energies.

---

[18]we refer to Fig. 3d and Fig. 4d. of Ref. (29).

Acknowledgement

References

[1] I. Arsene *et al.*, BRAHMS Collaboration, Nucl. Phys. **A 757**, 1 (2005).
[2] B.B. Back *et al.*, PHOBOS Collaboration, Nucl. Phys. **A 757**, 28 (2005).
[3] J. Adams *et al.*, STAR Collaboration, Nucl. Phys. **A 757**, 102 (2005).
[4] K. Adcox *et al.*, PHENIX Collaboration, Nucl. Phys. **A 757**, 184 (2005).
[5] J-Y. Ollitrault, Phys. Rev. **D 46**, 229 (1992).
[6] J. Barrette *et al.* E877 Collaboration, Phys. Rev. Lett. **73**, 2532 (1994).
[7] A.M. Poskanzer and S.A. Voloshin, Phys. Rev. **C 58**, 1671 (1998).
[8] H. Appelshäuser *et al.*, NA49 Collaboration, Phys. Rev. Lett. **80**, 4136 (1998).
[9] P. Huovinen, P.V. Ruuskanen, Ann. Rev. Nucl. Part. Sci. **56**, 163 (2006).
[10] M. Gyulassy, L. McLerran, Nucl. Phys. **A 750**, 30 (2005).
[11] T. Hirano, U. Heinz, D. Kharzeev, R. Lacey, Y. Nara, Phys. Lett.**B 636**, 299 (2006).
[12] K. Aamodt *et al.*, ALICE Collaboration, Phys. Rev. Lett. **105**, 252302 (2010).
[13] ATLAS Collaboration, Phys. Lett.**B 707**, 330 (2012).
[14] I. Tserruya, AIP Conf. Proc. 1422, 166 (2012), arXiv:1108.6018.
[15] M. Luzum, Phys. Rev.**C 83**, 044911 (2011).
[16] C. Shen, U. Heinz, P. Huovinen, H. Song, Phys. Rev.**C 84**, 044903 (2011).
[17] T. Hirano, P. Huovinen, and Y. Nara, Phys. Rev. **C 83**, 021902 (2011).
[18] C. Alt *et al.*, NA49 Collaboration, Phys. Rev. **C 68**, 034903 (2003).
[19] G. Agakichiev *et al.*, CERES Collaboration, Phys. Rev. Lett. **92**, 032301 (2004).
[20] M.M. Aggarwal *et al.*, WA98 Collaboration, Nucl. Phys. **A 762**, 129 (2005).
[21] P. Huovinen, P.F. Kolb, U. Heinz, P.V. Ruuskanen, S.A. Voloshin, Phys. Lett.**B 503**, 58 (2001).
[22] U. Heinz, J. .Phys. **G 31**, S717 (2005).
[23] U. Heinz, P. Kolb,J. Phys. **G 30**, S1229 (2004).
[24] D. Teaney, Phys. Rev. **C 68**, 034913 (2003).
[25] H. Niemi, G.S. Denicol, P. Huovinen, E. Molnar, D.H. Rischke, Phys. Rev. Lett. **106**, 212302 (2011).
[26] J. Milošević, CERES Collaboration, Nucl. Phys. **A 774**, 503 (2006);
J. Milošević, Universität Heidelberg, *Doctoral Thesis*, 2006.
[27] J. Slivova (now Bielčíková), Universität Heidelberg and Charles University in Prague, *Doctoral Thesis*, 2003.
[28] T. Hirano and M. Gyulassy, Nucl. Phys. **A 769**, 71 (2006).
[29] C. Shen, U. Heinz, Phys. Rev. **C 83**, 044909 (2011).
[30] S. Shi for the STAR Collaboration, arXiv:1201.3959; Private Communication S. Shi, 2011; B. Mohanty for the STAR Collaboration, J.Phys.G: Nucl.Part.Phys. **38**, 124023 (2011).
[31] A. Marín *et al.*, CERES Collaboration, J. Phys. **G 30**, S709 (2004).
[32] D. Adamova *et al.*, CERES Collaboration, Nucl. Instr. Meth. **A 593**, 203 (2008).
[33] P. Holl, P. Rehak, F. Ceretto, U. Faschingbauer, J.P. Wurm, A. Castoldi, E. Gatti,
Nucl. Instr. Meth. **A 377**, 367 (1996).
[34] S. Yurevich, Universität Heidelberg, *Doctoral Thesis*, 2006.
[35] S. Eidelman *et al.*, (Particle Data Group), Phys. Lett. **B 592**, 1 (2004).
[36] J. Podolanski and R. Armenteros, Phil. Mag. **45**, 13 (1954).
[37] W. Ludolphs (now Dubitzky), CERES Collaboration, Heidelberg University, *Doctoral Thesis*, 2006.
[38] P.M. Dinh, N. Borghini and J.-Y. Ollitrault, Phys. Lett. **B 477**, 51 (2000).
[39] D. Adamova *et al.*, CERES Collaboration, Nucl. Phys. **A 714**, 124 (2003).
[40] H. Tilsner, CERES Collaboration, Universität Heidelberg, *Doctoral Thesis*, 2002.
[41] G. Baym, P. Braun-Munzinger, Nucl. Phys. **A 610**, 124(1996).
[42] C. Alt *et al.*, NA49 Collaboration, Phys. Rev. **C 77**, 034906 (2008); http://na49info.web.cern.ch.

[43] Ch. Blume *et al.*, NA49 Collaboration, J. Phys.**G 35**, 044004 (2008).

[44] G. Stefanek *et al.*, NA49 Collaboration, PoS CPD2006:030 [arXiv:nucl-ex/0611003].

[45] C. Alt *et al.*, NA49 Collaboration, Nucl. Phys. **A 774**, 473 (2006).

[46] Private communication Ch. Blume, 2009

[47] S.V. Afanasiev *et al.*, NA49 Collaboration, Phys. Rev. **C 66**, 054902 (2002).

[48] M. Utvić, NA49 Collaboration, Universität Frankfurt, *Diploma Thesis*, 2006.

[49] Numerical Recipes in C, W.H. Press, S.A. Teukolski, W.T. Vetterling, B.P. Flannery, Cambridge University Press, 2nd edition, 1992.

[50] Y. Burnier, D.E. Kharzeev, J. Liao, and H.-U. Lee, Phys. Rev. Lett. **107**, 052303 (2011).

[51] V. Greco and C.M. Ko, Phys. Rev. **C 71**, 041901 (2005).

[52] D. Molnar and S.A. Voloshin, Phys. Rev. Lett. **91**, 092301 (2003).

[53] C. Nonaka, B. Müller, M. Asakawa, S.A. Bass, R.J. Fries, Phys. Rev. **C 69**, 031902 (2004).

[54] C. Markert for the STAR Collaboration, arXiv:0712.1838;
C. Markert, B. Bellwied, I. Vitev, Phys. Lett. **B 669**, 92 (2008).

[55] J.C. Dunlop, M.A. Lisa, and P. Sorensen (2011), Phys. Rev. **C 85**, 014910 (2012).

[56] D.E. Kharzeev, L.D.McLerran and H.J. Warringa, Nucl. Phys. **A 803**, 227 (2008).

[57] S.A. Voloshin, Phys. Rev. **C 70**, 057901 (2004).

[58] M. Oldenburg *et al.*, STAR Collaboration, J. Phys.**G 32**, S563 (2006).

[59] P. Huovinen (private communications), 2005.

[60] J. Adams *et al.*, STAR Collaboration, Phys. Rev. **C 72**, 014904 (2005).

[61] T. Hirano, Phys. Rev. **C 65**, 011901(R) (2002).

[62] J. Adams *et al.*, STAR Collaboration, Phys. Rev. Lett. **92**, 052302 (2004).

[63] C. Alt *et al.*, NA49 Collaboration, Phys. Rev. **C 75**, 044901 (2007).

[64] B.I. Abelev *et al.*, STAR Collaboration, Phys. Rev. **C 77**, 054901 (2008).

[65] E. Schnedermann, J. Sollfrank, U. Heinz, Phys. Rev. **C 48**, 2462 (1993).

[66] C. Shen, U. Heinz, P. Huovinen, H. Song, Phys. Rev. **C 82**, 054904 (2010).

[67] D. Molnar, J. Phys. **G 38**, 124173 (2011).